

# RESONANT SCATTERING EFFECT ON THE SOFT X-RAY LINE EMISSION FROM THE HOT INTERSTELLAR MEDIUM: I. GALACTIC BULGES

YANG CHEN<sup>1,2</sup>, Q. DANIEL WANG<sup>3</sup>, GAO-YUAN ZHANG<sup>1</sup>, SHUINAI ZHANG<sup>3,4</sup>, AND LI JI<sup>4</sup>

*Draft version March 23, 2022*

## ABSTRACT

Diffuse soft X-ray line emission is commonly used to trace the thermal and chemical properties of the hot interstellar medium, as well as its content, in nearby galaxies. Although resonant line scattering complicates the interpretation of the emission, it also offers an opportunity to measure the kinematics of the medium. We have implemented a direct Monte Carlo simulation scheme that enables us to account for resonant scattering effect in the medium, in principle, with arbitrary spatial, thermal, chemical, and kinematic distributions. Here we apply this scheme via dimensionless calculation to an isothermal, chemically uniform, and spherically symmetric medium with a radial density distribution characterized by a  $\beta$ -model. This application simultaneously account for both optical depth-dependent spatial distortion and intensity change of the resonant line emission due to the scattering, consistent with previous calculations. We further apply the modeling scheme to the OVII and OVIII emission line complex observed in the *XMM-Newton* RGS spectrum of the M31 bulge. This modeling, though with various limitations due to its simplicity, shows that the resonant scattering could indeed account for much of the spatial distortion of the emission, as well as the relative strengths of the lines, especially the large forbidden to resonant line ratio of the OVII He $\alpha$  triplet. We estimate the isotropic turbulence Mach number of the medium in M31 as  $\sim 0.17$  for the first time and the line-emitting gas temperature as  $\sim 2.3 \times 10^6$  K. We conclude that the resonant scattering may in general play an important role in shaping the soft X-ray spectra of diffuse hot gas in normal galaxies.

*Subject headings:* X-rays: galaxies — galaxies: bulges — galaxies: individual (M31) — X-rays: ISM — ISM: lines and bands — radiative transfer

## 1. INTRODUCTION

The hot interstellar medium (ISM) represents a key component of the galactic ecosystem in disk galaxies similar to our own. In particular, the medium bears direct imprints of stellar feedbacks, both energetical and chemical, which are an essential ingredient that is yet to be understood in the theory of galaxy formation and evolution. With a characteristic temperature of  $\gtrsim 10^6$  K, the medium can be well traced by soft X-ray emission, which is dominated by various lines from K- or L-shell transitions of heavy elements such as O, Ne, and Fe ions (e.g., OVII, OVIII, NeIX, and FeXVII). The emission is commonly assumed to be optically thin in spectral modeling. However, this assumption may not hold for certain resonant lines, which depend on their oscillation strengths, the thermal broadening and turbulent velocity dispersion and density of the hot gas, and the abundances and ionization states of the elements.

A photon in a resonant line can be absorbed and then re-emitted by a suitable ion in different directions. In such a resonant “scattering” (RS) event, the energy of this photon is shifted, mainly due to the turbulent and thermal random motions of the ion. Statistically and cumulatively, this shift tends to be away from the line center, where the optical depth is the highest, and in-

creases the chance for the photon to escape from the medium. The resultant line broadening is sometimes called Zanstra effect (see, e.g., Zanstra 1949; Field 1959), the direct measurement of which, however, demands very high spectral resolution observations. With the existing X-ray instruments, we can detect the spatial distortion of the surface intensity distribution of the line emission due to the RS effect. The degree of this distortion is optical depth-dependent; the observed line photons primarily escape from outer regions of the medium, which are optically thin to the line. The relative intensities of various emission lines are altered in a spectrum extracted from a fixed field covering only part of the medium. In addition, the RS increases the accumulated propagation path length of a photon and hence its probability for being absorbed photoelectrically by cool gas if it coexists with the hot medium. Accounting for these effects is thus essential for the measurements of the thermal and chemical properties of the medium, which are sensitive to the line intensities. Incidentally, the line optical depth dependence of the RS effects can provide us with a powerful tool to constrain the kinematic state of the medium.

The RS effect in X-rays has been studied mostly in diffuse hot plasma of massive elliptical galaxies and clusters of galaxies (e.g., Xu et al. 2002; Sazonov, Churazov, & Sunyaev 2002; Churazov et al. 2004; Molnar, Birkinshaw, & Mushotzky 2006; Werner et al. 2009; Zhuravleva et al. 2011; Ogorzalek et al. 2017; Hitomi Collaboration et al. 2018). The spectra of diffuse X-ray emission from such systems typically show distinct iron emission lines from K-shell and L-shell transitions. The relative intensities of the emission lines of vastly different opacities, arising from different transitions of the same species (e.g., Fe

<sup>1</sup> Department of Astronomy, Nanjing University, 163 Xianlin Avenue, Nanjing 210023, P.R.China

<sup>2</sup> Key Laboratory of Modern Astronomy and Astrophysics, Nanjing University, Ministry of Education, P.R.China

<sup>3</sup> Department of Astronomy, B619E-LGRT, University of Massachusetts, Amherst, MA01003

<sup>4</sup> Purple Mountain Observatory, 8 Yuanhua Road, Nanjing 210034, P.R.China

XVII 15 and 17 Å lines), have effectively been used to infer the turbulent Mach numbers in the plasma, which are up to a few tenths. The earliest theoretical work by Gilfanov, Syunyaev, & Churazov (1987) is based on an iteration method to estimate the radiative transfer equation, assuming an isothermal spherical  $\beta$ -model gas distribution, and neglecting the photo-electric absorption by cool gas, which might be intermixed with the hot medium. Later works typically use the Monte Carlo (MC) radiative transfer simulations of the resonant scattering effect on lines typical for the  $\gtrsim 10^7$  K gas (see, e.g., the other references mentioned in this paragraph).

In disk galaxies, the RS can also be important, although its effects may not be separated easily from other physical processes in the hot ISM. The characteristic temperature of the hot ISM is  $\sim 10^{6.3}$  K, as estimated from existing X-ray absorption and emission observations (e.g., Wang 2010). At such a temperature, the medium is expected to produce strong line emission from K-shell transitions in H-like and He-like ions, such as OVIII, OVII, NeX, and NeIX, as well as those Fe L-shell ones (e.g., Wang 2010; Porquet et al. 2010; Foster et al. 2012). Although the collisional ionization equilibrium (CIE) is often *assumed* for the hot ISM, complications can arise from non-CIE processes such as the photo-ionization by recent or ongoing AGN activity (e.g., Segers et al. 2017) and the charge exchange (CX) between ions and neutral atoms at the interface with cool gas (Ranalli et al. 2008; Liu et al. 2010, 2011; Zhang et al. 2014), as well as the over-heating (e.g., due to recent shock-heating) or over-cooling (e.g., fast adiabatic expansion; e.g., Breitschwerdt & Schmutzler 1999). These processes, which could be common in the dynamic (or violent) hot ISM of star-forming disk galaxies, are important to study.

Despite these potential complications, observational signs of significant RS effects are present for nearby disk galaxies, including our own. X-ray *absorption* line spectroscopy of bright background point-like sources reveals that the hot ISM in our Galaxy is optically thick to the resonant line of the OVII He $\alpha$  triplet (e.g., Wang et al. 2005). The RS by the foreground hot ISM is also used to explain the emission line intensity ratios observed in the *Suzaku* spectrum of the North Polar Spur (Gu et al. 2016). The *XMM-Newton* RGS study of the bulge of M31 shows that the forbidden to resonant line ratio of the OVII He $\alpha$  triplet is much greater than 1, as would be expected from a hot CIE plasma (Liu et al. 2010; Zhang et al. 2018a, in prep). There is no significant massive star formation or ongoing AGN activity in the bulge, which contains only a small amount of cool gas, mainly confined in the inner 200 pc. In such a “quiescent” environment, a significant CX is not expected<sup>5</sup>. Can the RS play a role? Based on existing studies (Li et al. 2009; Liu et al. 2010), we find that the inner bulge region of M31 could indeed be substantially optically thick in strong resonant

<sup>5</sup> Liu et al. (2010) qualitatively considered CX as an interpretation of the enhanced OVII K $\alpha$  forbidden line. This interpretation seems to be consistent with the similarity between the radial intensity distributions of the line and the H $\alpha$  emission in the inner bulge of M31. But, quantitatively, the interpretation might have difficulties, because the interface between the cool and hot gases in the M31 inner bulge, where H $\alpha$  emission is confined in a flattened spiral structure (Dong et al. 2016), is likely to be substantially small and weakly turbulent (Zhang et al. 2018a in prep).

lines of OVII, OVIII, and FeXVII, for example, depending largely on how small the turbulent velocity of the diffuse hot ISM is. This dependence can in turn be used to estimate the velocity, which is crucially needed for the study of the energetics and dynamics of the hot ISM.

The RS effect on the X-ray spectroscopic properties of the hot ISM in disk galaxies has not been well explored yet since the modeling is somewhat challenging. The optical depth is too large ( $\gtrsim 1$ ) for the RS to be treated as a simple correction, but is not large enough to be considered as a diffusion problem. The mean free path of line photons could be comparable to, or even larger than, the characteristic length scale of the hot ISM. Thus MC simulations should be an optimal approach to quantify the RS effects, allowing for complications due to various spatial, thermal, chemical, and kinematical properties of the hot ISM. Indeed, this MC approach has been used successfully for similar radiative transfer problems (e.g., Ahn, Lee, & Lee 2000; Zheng & Miralda-Escudé 2002; Cantalupo et al. 2005; Dijkstra, Haiman, & Spaans 2006a,b) and especially in dealing with the RS effect on the X-ray emission of hot intracluster gas (e.g., Sazonov et al. 2002; Churazov et al. 2004; Molnar et al. 2006; Werner et al. 2009; Zhuravleva et al. 2010; Zhuravleva et al. 2011; de Plaa et al. 2012; Zhuravleva et al. 2013; Ogorzalek et al. 2017) over a decade or two.

In this paper we present our calculation scheme of the MC simulation for the radiative transfer of the resonant lines in hot gas, the spatial distribution of which is characterized by the  $\beta$ -model. We largely follow the formalism described in Dijkstra et al. (2006a) and Zheng & Miralda-Escudé (2002) for the RS of hydrogen Ly $\alpha$  photons and adapt it to the RS of the soft X-ray line emission from the hot ISM. We describe the scheme in some algorithmic details, which incorporates a finite boundary, as well as the transformation between the ion’s rest frame and the laboratory frame and the ion velocity-dependent probability and recoil effect of the RS. Our focus here is on an application of the scheme to a simple case, in which the hot ISM is assumed to be isothermal, chemically uniform, and spherically symmetric. This application allows us to directly compare some of our results with those obtained by the iterative method (Gilfanov et al. 1987) and apply them to the analysis of the RGS data on the inner bulge of M31. In subsequent papers, we will explore more sophisticated cases (e.g. Zhang et al. 2018b in prep, Paper II), including the RS in non-spherical asymmetric gaseous spheroids or disks, the effect due to photo-electric absorption, and the inclination angle dependence, as well as the different viewing perspectives, internal or external to the medium.

The rest of the present paper is organized as follows: In § 2, we describe the modelling and the MC algorithm for the RS in the hot ISM of galactic bulges. We present our test simulations in § 3 and an application to the X-ray spectrum of the M31 bulge in § 4. We discuss the results in § 5 and summarize this work in § 6.

## 2. RESONANT SCATTERING MODELING

### 2.1. Fundamentals

A key factor in determining the effectiveness of the RS is the motion of ions in the hot ISM. We assume that the

TABLE 1  
THE LINE PROPERTIES AND OPTICAL DEPTHS FITTED TO THE DATA

Ion ( $\lambda_{\text{rest}}$ ) [Å]	transition	$f_{lu}$	$\Gamma$ $\text{s}^{-1}$	$w_I : w_D$	$\tau^\dagger$	
O VIII Ly $\alpha$ (18.967)	$2p^2P_{3/2}-1s^2S_{1/2}$	0.28	$2.566 \times 10^{12}$	1/2:1/2	4.80	4.19
O VIII Ly $\alpha$ (18.973)	$2p^2P_{1/2}-1s^2S_{1/2}$	0.14	$2.564 \times 10^{12}$	1:0	2.40	2.09
O VII K $\beta$ (18.627)	$1s3p^1P_1-1s^2^1S_0$	0.16	$1.010 \times 10^{12}$	0:1	1.70	1.49
O VII r (21.602)	$1s2p^1P_1-1s^2^1S_0$	0.72	$3.430 \times 10^{12}$	0:1	9.04	7.88
O VII i (21.804)	$1s2p^3P_0-1s^2^1S_0$	$8.2 \times 10^{-5}$	$3.830 \times 10^8$			$\sim 0$
O VII f (22.098)	$1s2s^3S_1-1s^2^1S_0$	$2.0 \times 10^{-10}$	$9.120 \times 10^2$			$\sim 0$

NOTE. — The line properties are taken from AtomDB v3 (Foster et al. 2012).  $f_{lu}$  is the transition oscillator strength,  $\Gamma$  is the natural broadening damping factor, and “ $w_I : w_D$ ” represents the weight ratio between isotropic scattering and dipole scattering.

$\dagger$  The right (left) column of  $\tau$  values is for the case where turbulence is (not) taken into account.

motion consists of a thermal component and an isotropic turbulent component and that their combined velocity follows a Gaussian distribution in each dimension:

$$P_v(v) dv = \frac{1}{\sqrt{2\pi}\sigma_v} \exp\left[-\frac{1}{2}\left(\frac{v}{\sigma_v}\right)^2\right] dv. \quad (1)$$

Here, the velocity dispersion is given by

$$\sigma_v = \sqrt{\sigma_{\text{th}}^2 + \sigma_{\text{tu}}^2}, \quad (2)$$

where  $\sigma_{\text{th}} = (kT/\mu_a m_p)^{1/2}$  and  $\sigma_{\text{tu}}$  are the thermal and turbulent velocity dispersions, while  $\mu_a$  and  $m_p$  are the ion species’ atomic weight and the proton mass, respectively. Accordingly, seed photons are emitted with the frequencies following a distribution profile:

$$P_\nu(\nu) d\nu = \frac{1}{\sqrt{2\pi}\sigma_\nu} \exp\left[-\frac{1}{2}\left(\frac{\nu - \nu_0}{\sigma_\nu}\right)^2\right] d\nu, \quad (3)$$

where  $\sigma_\nu = \nu_0(\sigma_v/c)$  is the standard deviation in frequency  $\nu$  around the center frequency  $\nu_0$  of the line, while  $c$  is the speed of light.

The absorption cross-section of the photons is a result of the Lorentz profile of the line convolved with the Doppler shift (e.g., Mihalas 1978):

$$s(x) = \frac{\sqrt{\pi}e^2}{m_e c \Delta\nu_D} f_{lu} H(a, x), \quad (4)$$

where  $f_{lu}$  is the oscillation strength of the lower to upper level transition in the consideration,  $\Delta\nu_D = \nu_0(\sqrt{2}\sigma_v/c)$  is the Doppler width, and the Voigt function is defined as

$$H(a, x) \equiv \frac{a}{\pi} \int_{-\infty}^{\infty} \frac{\exp(-u^2)}{(x-u)^2 + a^2} du, \quad (5)$$

with  $a = \Gamma/(4\pi\Delta\nu_D)$  the Voigt parameter ( $\Gamma$  is the damping width, equal to the spontaneous emission rate  $A_{ul}$ ),  $x \equiv (\nu - \nu_0)/\Delta\nu_D$  the dimensionless frequency shift, and  $u$  the atomic line-of-sight velocity component in units of  $\sqrt{2}\sigma_v$  (which is also equal to the Doppler frequency shift in units of  $\Delta\nu_D$ ). Table 1 lists the parameters of the strongest oxygen lines used in the application presented in the next section.

The Voigt function has an approximate profile  $\exp(-x^2)$  in the line core and approaches the asymptotic curve  $a/(\sqrt{\pi}x^2)$  in the line wing (e.g., Mihalas 1978; Dijkstra et al. 2006a). For the sake of saving calculation

time in this work, the Voigt function is approximated as

$$H(a, x) \approx \exp(-x^2) + \frac{a}{\pi^{1/2}x^2} [1 - \exp(-x^2)], \quad (6)$$

with a small modification to the approximation given in Mihalas (1978), namely adding the artificial terms in the square brackets to avoid the divergence at the line center.

The RS is only partially coherent in the observer’s frame because of the ion’s motion (Dijkstra et al. 2006a). The frequency of the scattered photon is given by

$$x_f \approx x_i - \frac{\mathbf{v}_a \cdot \mathbf{k}_i}{\sqrt{2}\sigma_v} + \frac{\mathbf{v}_a \cdot \mathbf{k}_f}{\sqrt{2}\sigma_v} + g(\mathbf{k}_i \cdot \mathbf{k}_f - 1), \quad (7)$$

where  $\mathbf{k}$  is the unit vector of the photon’s propagating direction, the subscripts “ $i$ ” and “ $f$ ” denote the quantities of the incident and scattered photons, respectively,  $\mathbf{v}_a$  is the velocity of the atom (ion), and  $g = h\Delta\nu_D/(2\mu_a m_p \sigma_v^2)$  is the average fraction of energy transferred per scattering to the ion due to its recoil. For the O VII resonant line,  $g = 8 \times 10^{-5}(\sigma_v/100 \text{ km s}^{-1})^{-1}$ , which is negligible by orders of magnitude.

## 2.2. Distribution model of the Hot ISM

Our simulation scheme is meant to be applicable to any spatial distribution of the hot ISM in terms of its thermal, chemical, and kinematic properties. In principle, the distribution could even be derived from a galaxy simulation. But in the present work, we adopt a simple model of the medium with certain symmetry and uniformity to characterize the effects of the RS. For such a model, we may define an optical depth at the line center of each transition,  $\tau = \int n_{\text{ion}}(Z) s(0) dr$ , to characterize the systemic radiative transfer condition of the gas. The integration here is from the center of the galaxy to the infinity or to a sufficient large off-center distance  $r_{\text{cut}}$ , beyond which the optical depth contribution is negligible. Ions responsible for the RS are assumed to be populated in the ground states. The ion number density of an element  $Z$ ,  $n_{\text{ion}}(Z)$ , is related to the hydrogen density as  $n_{\text{ion}}(Z) = \zeta(Z) A(Z) f_{\text{ion}}(T) n_{\text{H}}$ , where  $A(Z)$  is the solar photosphere elemental abundance with respect to hydrogen (H),  $\zeta(Z)$  is the hot ISM elemental abundance relative to solar, and  $f_{\text{ion}}(T)$  is the ionic fraction of the element as a function of the gas temperature. For oxygen,  $A(\text{O}) = 8.51 \times 10^{-4}$  (Anders & Grevesse 1989). In this work, we calculate  $f_{\text{ion}}(T)$  via the APEC model, assuming the CIE for the hot ISM.

The key parameter that determines the effectiveness of the RS is the line-center optical depth  $\tau$ . In terms of determining the energy (i.e.,  $x$ ) distribution of the line photons emerging from the medium,  $\tau$  encapsulates the dependence of the RS on the density, size of the considered region, the temperature, the elemental abundance, and the ionic fraction of the hot ISM, as well as its turbulent velocity. In particular,  $\tau$  is inversely proportional to the velocity dispersion  $\sigma_v$ . The additional dependence of the distribution on  $a$  in the second term of Eq. (6) and on  $\sigma_v$  in the last term of Eq. (7) are orders of magnitude weaker<sup>6</sup> than the other right-hand side terms of the equations and can generally be neglected. The decisive dependence of the RS effect on  $\tau$  will be shown below.

The spatially resolved effect of the RS bears on the specific distribution of the hot ISM. In the present work, we will use the isothermal  $\beta$ -model (see Cavaliere & Fusco-Fermiano 1978; Arnaud 2009):

$$n_{\text{H}} = n_0 \left[ 1 + \left( \frac{r}{r_c} \right)^2 \right]^{-3\beta/2}, \quad (8)$$

where  $n_0$  is the gas density at the spherical center and  $r_c$  the core radius. With this model, the total radial optical depth is the natural choice

$$\tau(x) \equiv \int_0^\infty n_{\text{ion}}(Z) s(x) dr. \quad (9)$$

It can be transformed to

$$\tau(x) = \tau_c H(a, x) \int_0^\infty (1 + \tilde{r}^2)^{-3\beta/2} d\tilde{r}, \quad (10)$$

where  $\tau_c \equiv n_{\text{ion},0}(Z) s(0) r_c$ , with  $n_{\text{ion},0}(Z)$  denoting the ion density at  $r = 0$ ,  $\tilde{r} \equiv r/r_c$ , and the integral has an analytic solution  $\sqrt{\pi}[\Gamma(3\beta/2 - 1/2)/2\Gamma(3\beta/2)]$ , with  $\Gamma$  the gamma function, for  $\beta > 1/3$  (Ge et al. 2016).

### 2.3. MC simulations

In our MC simulations, seed photons are generated with random directional angles and with the location probability according to the volume emissivity distribution of the hot ISM. For the isothermal and chemically uniform medium of a spherically symmetric distribution assumed in the present work, the positional angle of a seed photon is random, while its radius  $r$  is found from the probability distribution function

$$R_1 = \frac{\int_0^r n_e n_{\text{ion}}(Z) r'^2 dr'}{\int_0^{r_{\text{cut}}} n_e n_{\text{ion}}(Z) r'^2 dr'}, \quad (11)$$

where  $R_1 \in [0, 1]$  is a randomly generated number, and  $n_e$  is the electron density. The frequency of this photon is generated according to Eq. (3). For the  $\beta$ -model distribution, Eq. (11) can be simplified as

$$R_1 = \frac{\int_0^{r/r_c} G(y) dy}{\int_0^{r_{\text{cut}}/r_c} G(y) dy}, \quad G(y) = \frac{y^2}{(1 + y^2)^{3\beta}}. \quad (12)$$

An advantage of the MC simulation is that one can “trace” a resonant line photon at each step in their random traveling. In the simulation we use an optical depth

<sup>6</sup> For example,  $a = 1.2 \times 10^{-2}$  for the 21.602Å O VII resonant line at  $kT = 0.2$  keV.

step  $\Delta\tau(x)/\tau_c$ , where  $\Delta\tau(x) \equiv n_{\text{ion}}(Z) s(x) \Delta l$ , to determine the adaptive spatial length step  $\Delta l$  along a given random direction of photon propagation. With a sufficiently small  $\Delta\tau(x)$ , the hot ISM can be assumed to be uniform in each step. For the gas with a similarity distribution like the  $\beta$ -model (Eq. 8), the spatial stepsize can be given in a dimensionless form:

$$\frac{\Delta l}{r_c} = \left[ 1 + \left( \frac{r}{r_c} \right)^2 \right]^{3\beta/2} \frac{\Delta\tau(x)}{\tau_c} H^{-1}(a, x). \quad (13)$$

The spatial stepsize and the pathlength of the photon before each scattering (which can be a sum of small steps) are thus dominated by  $\tau_c$ , which is actually controlled by the total radial optical depth  $\tau(x)$  (or the line-center  $\tau$  for  $x = 0$ ) through Eq.(10).

After propagating each step, the photon is checked to see whether a scattering happens. If the scattering probability  $1 - \exp(-\Delta\tau(x))$  is smaller than a randomly generated number  $R_2 \in [0, 1]$ , then no RS is declared and the photon moves a step forward along the present direction, which may continue until it escapes or moves outside the boundary of the system. Otherwise, a RS event is flagged, in which a photon is re-emitted in a new direction.

Each RS event changes not only the energy of the photon (Eq. 7) but also its direction. These changes depend on the velocity of the scattering ion, which consists of three components: the one parallel to the direction of the incident photon,  $\mathbf{k}_i$ , and the two mutually orthogonal ones perpendicular to  $\mathbf{k}_i$ . Following the method described in Zheng & Miralda-Escudé (2002, also see the Appendix therein), we randomly generate the parallel component following the distribution

$$f(u_{\parallel}) = \frac{a}{\pi} \frac{e^{-u_{\parallel}^2}}{(x_i - u_{\parallel})^2 + a^2} H^{-1}(a, x_i), \quad (14)$$

where  $u_{\parallel}$  is in unit of  $\sqrt{2}\sigma_v$ . This distribution accounts for the RS probability as a function of  $u_{\parallel}$  and  $x_i$ . Each perpendicular component is generated from a Gaussian distribution with zero mean and standard deviation  $\sigma_v$ .

The redirection of the scattered photon can be treated as a mixture of isotropic scattering (with a weight  $w_{\text{I}}$ ) and Rayleigh (dipole) scattering (with a weight  $w_{\text{D}}$ ), and the weighted probability distribution is given by (Hamilton 1947; Churazov et al. 2010)

$$R_3 = \int_{-1}^{\mu} \left[ \frac{1}{2} w_{\text{I}} + \frac{3}{8} (1 + \mu'^2) w_{\text{D}} \right] d\mu', \quad (15)$$

where  $R_3$  is a random number  $\in [0, 1]$  and  $\mu$  is the cosine of the angle between the incident and outgoing directions of the photon. The weights  $w_{\text{I}}$  and  $w_{\text{D}}$  for the considered oxygen lines are given in Table 1. The relevant quantities are treated by coordinate rotation and Lorentz transformation between the observer’s frame and the atom’s rest frame in which the incident direction is the symmetric axis.

We record all the positions, directions, and energy information of simulated photons from their initial emission through all RS events before escaping from the system. This complete record allows for the post-processing of the simulation, even with the inclusion of additional

processes such as photo-electric absorption by cool gas, and for generating mock observations, as will be demonstrated in the follow-up paper (Paper II).

For the resonant line emission of the hot gas, the terms with  $a$  and  $g$  are negligible in the Voigt function (6) (hence also in the dimensionless positions of the photon (Eq. 13)) and the photon frequency change (Eq. 7), respectively. Therefore, the MC simulation in terms of dimensionless frequencies and dimensionless lengths, with the characteristic  $\tau$  given, is essentially *irrespective of specific lines and the gas velocity dispersion*.

### 3. TEST SIMULATIONS AND RESULTS

We run a set of simulations for a spherical  $\beta$  model distribution of gas to test our scheme, compare the calculation with the existing iterative algorithm, and make new application to the RGS data of the M31 bulge. The diffuse soft X-ray emission from the bulge is well characterized with model parameters  $\beta = 0.5$ ,  $r_c = 54''$  (or 0.2 kpc at a distance 780 kpc), and  $n_0 \sim 0.1 \text{ cm}^{-3}$  (Liu et al. 2010; Li et al. 2009). We adopt an outer boundary at  $r_{\text{cut}} = 100r_c$ , which is typically far beyond region where the gas distribution can be modeled or the spectral data can be extracted (§4). The outer region ( $r > r_{\text{cut}}$ ) would contribute only a small fraction (less than a few percent) of the total optical depth integrated to infinity (see Fig. 1). Considering the drastic change of gas density at various radii in the  $\beta$ -model, an upper cutoff  $\Delta l_{\text{max}}/r_c = 0.01$  is set for the stepsize while  $\Delta\tau(x)/\tau_c = 0.001$  is used.

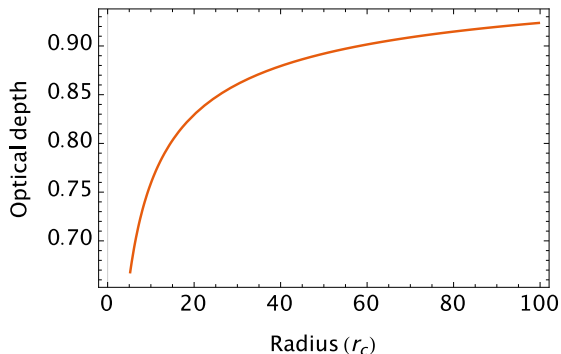


FIG. 1.— Scaled radial line-center optical depth  $\tau$  (in units of the maximum value at  $\infty$ ) of the adopted  $\beta$ -model hot gas ( $\beta=0.5$ ) as a function of the dimensionless radius over which the integration is made from the center of M31 (see §3 for details).

We first carried out a test simulation assuming a  $\beta$ -model of gas with  $\beta = 2/3$ . This simulation is used for the comparison with the calculation under the iterative method introduced by Gilfanov (1987) (see Appendix A). For the comparison of the two methods, some treatments in our simulations are simplified (instead of those described in §2). As shown in Appendix A, the radial surface profiles and the line profiles produced with the MC simulation are consistent with those produced with the iterative method for representative  $\tau$  values. We note that iterative results from Gilfanov et al. (1987) have been compared to the results of MC simulations in previous works (e.g., Sazonov et al. 2002 and consequent papers); our test is in essence also consistent with the previous MC results.

We then run simulations with the considerations described in §2 for a  $\beta$ -model of the hot plasma distribution suitable for the M31 bulge. Parameters  $a$  and  $g$  for the OVII resonant line at  $kT = 0.2 \text{ keV}$  are used, although the last terms in both Eq.(6) and Eq.(7) are essentially negligible. For each simulation, if not specially stated,  $10^6$  photons are run as a compromise between a reasonably good statistical quality and a moderate computational time.

Fig. 2 presents line profiles of the photons emerging from the RS for various representative optical depth values from the entire galaxy and from within the projected central  $5r_c$  radius, respectively. Both isotropic and dipole scattering cases are shown. For the same  $\tau$ , the line profiles differs very slightly between the two cases. In each case, the line profile, as an explicit function of  $x$  (other than of  $\nu$ ), changes only with  $\tau$ . With the increase of  $\tau$ , the core of the line gets increasingly reduced while the wing widens. Such effect is more evident in the inner region (right panel of Fig.2), where double-peak pattern appears when  $\tau \gtrsim 5$ .

Fig. 3 represents the radial surface brightness profiles of the resonant line for various  $\tau$  values. The brightness profiles are shown for both isotropic and dipole scatterings: there is almost no difference between the two cases, however. With the increase of  $\tau$ , the brightness in the central projected region within  $5\text{--}10r_c$  (1–2 kpc) drops, while the emission from the outer region is enhanced. Both distortions are the results of the RS-resultant random walk of photons in space.

Fig. 4 gives the radial profiles of the equivalent width (EW) of the resonant line emission relative to the ones for  $\tau = 0$ . With increasing  $\tau$ , the EW diminishes in the central projected region and rises in the outskirts, which reflects the behavior of the line emission brightness.

The spatial redistribution of resonant line photons accordingly changes the specific intensity of the line and hence the surface distribution of the diagnostic G-ratio for the so-called  $K\alpha$  (or  $\text{He}\alpha$ ) triplet of a helium-like ion, such as OVII. The G-ratio is defined as the ratio of the sum of intercombination and forbidden components to the resonant component (Gabriel & Jordan 1969). Fig. 5 shows the radial profiles of the G-ratio for the  $\beta$ -model gas for various  $\tau$  values, which are relative to the ones for  $\tau = 0$ . Due to the RS effect, G-ratio can be considerably elevated (e.g., a few times) in the central projected region and diminished (even by half) in the outskirts. Ideally, the G-ratio of the OVII triplet is close to 1 for a hot CIE gas at  $\sim 2 \times 10^6 \text{ K}$  which typifies the temperature of the M31 bulge (see §4). Therefore, the RS effect may raise the OVII G-ratio to a value substantially higher than 1 within a few  $r_c$  and suppress it to below 0.5 near the boundary.

## 4. APPLICATION TO THE RGS SPECTRUM OF THE M31 BULGE

### 4.1. RGS Data Reduction

Based on the above results (e.g., Fig. 3), we further build a spectral model to account for the RS effect, allowing for a direct fit to an RGS spectrum. The RGS is a slit-less spectrometer and is sensitive to photons in the 0.3–2 keV range. For a point-like source, the spectral resolution of the RGS is  $\lambda/\delta\lambda \sim 400$  at  $\sim 20 \text{ \AA}$  (for details, please refer to the *XMM-Newton* Users' Handbook). For

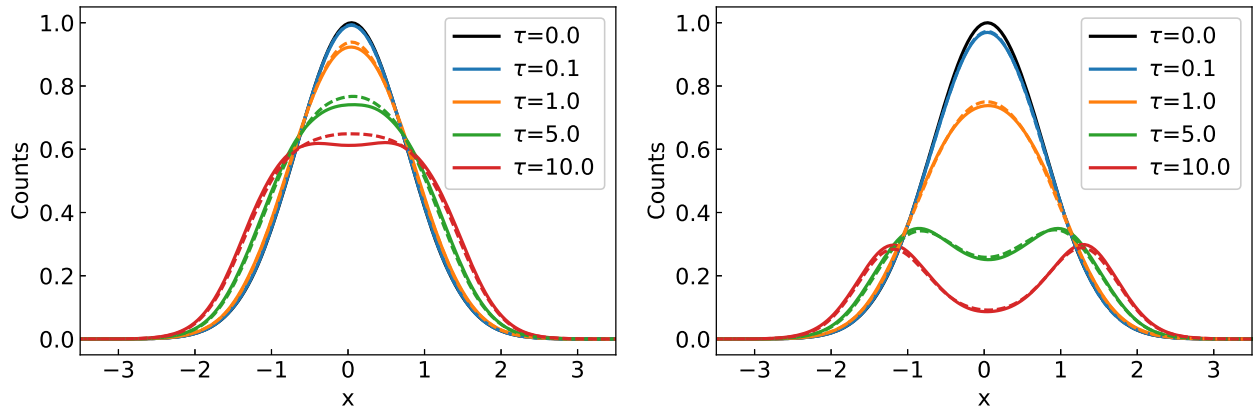


FIG. 2.— *Left*: Line profiles of resonant photons from the  $\beta$ -model gas with  $\beta = 0.5$  and  $r_{\text{cut}} = 100r_c$  for various  $\tau$  values. The dashed and solid lines are for isotropic and dipole scatterings (in the atom’s rest frame), respectively. *Right*: Same as in the left panel except for photons emerging only from within the inner region of a projected radius  $5r_c$ . A 3-pixel ( $x$  interval of 0.13) Gaussian smoothing is applied to reduce the noise of the simulated data.

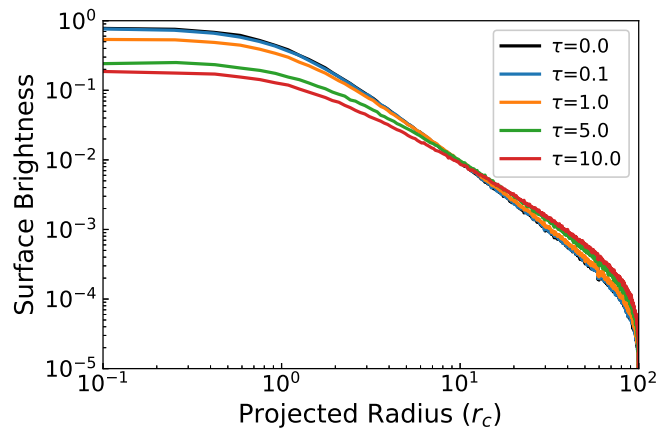


FIG. 3.— Projected radial surface brightness profiles of the hot gas line emission predicted by the adopted  $\beta$ -model with  $\beta = 0.5$  and  $r_{\text{cut}} = 100r_c$  for various  $\tau$  values.

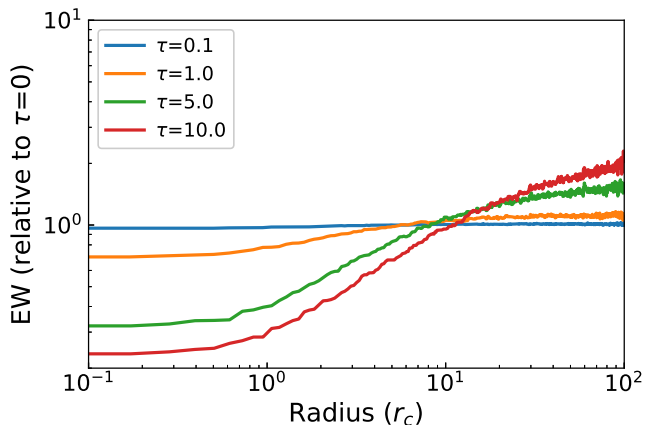


FIG. 4.— Projected radial profiles of the equivalent width of the line emission predicted by the  $\beta$ -model with  $\beta = 0.5$  and  $r_{\text{cut}} = 100r_c$ , scaled with the profile of  $\tau = 0$ .

an extended source, one may directly obtain useful 1-D spatial information over a width of  $5'$  in the cross-dispersion direction. In the dispersion direction, the RGS covers the entire field of view of the telescope mirrors, although the effective area decreases significantly at large off-axis angles. A spatial displacement along the dis-

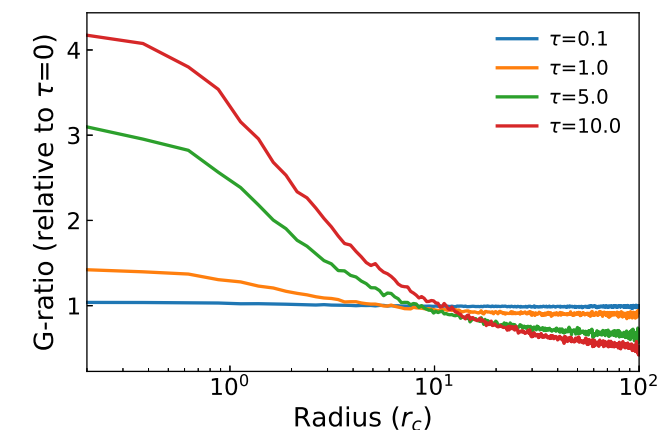


FIG. 5.— Projected radial profiles of the  $K\alpha$  triplet G-ratio of helium-like ions as predicted by the  $\beta$ -model with  $\beta = 0.5$  and  $r_{\text{cut}} = 100r_c$ , scaled with the profile of  $\tau = 0$ .

persion direction translates to an apparent (1st-order) wavelength shift of  $0.138 \text{ \AA}$  per arcmin. Therefore, for an emission region with a moderate extent (e.g.,  $\lesssim 2'$ ), its integrated RGS spectrum still has a spectral resolution substantially better than that of X-ray CCD data.

Table 2 lists 36 *XMM-Newton*/RGS observations toward the bulge region of M31, whose dispersion directions and the widths of extracting regions ( $\sim 4'$ , or 920 pc) are shown in Fig. 6. The Science Analysis System (SAS, v14.0) and current calibration files are used for the data reduction. After removing the intense background-flare periods, the remaining total effective exposure time is 766 ks. We use the standard ‘*rgsproc*’ script to extract the RGS spectra of individual observations of M31 (R.A. =  $00^{\text{h}}42^{\text{m}}44^{\text{s}}.237$  and Dec. =  $+41^{\circ}16'11''.63$ , J2000) as a common dispersion reference position. The corresponding background spectra are generated from blank-sky events. These spectra from individual observations are combined with the ‘*rgscombine*’ script.

#### 4.2. Spectral analysis

To study the diffuse hot gas, we also need to estimate the contribution from two unrelated components in the bulge: (1) bright point sources, mostly low-mass X-ray binaries, and (2) weak unresolved point sources,

TABLE 2  
36 XMM-NEWTON/RGS OBSERVATIONS ON M31'S CENTER  
(2000-2012)

ID	RA	Dec	P.A.	$t_{Exp}$	$t_{eff}$
0109270101	10.680324	41.266006	76.1	57.9	33.5
0109270501	10.680122	41.266124	76.1	10.6	4.7
0112570101	10.679958	41.259701	249.9	64.3	62.8
0112570401	10.679071	41.266209	78.3	46.0	33.9
0112570601	10.680028	41.260037	257.0	13.3	13.0
0112570701	10.680006	41.259403	249.9	4.5	3.3
0405320501	10.685502	41.272990	71.7	21.9	20.3
0405320601	10.684280	41.273203	51.3	21.9	19.1
0405320701	10.686068	41.265342	252.4	15.9	15.9
0405320801	10.685275	41.265725	243.2	13.9	13.9
0405320901	10.685723	41.266047	231.8	16.9	16.9
0505720201	10.685294	41.265129	253.8	27.5	27.5
0505720301	10.684693	41.266217	247.9	27.2	27.1
0505720401	10.685944	41.265534	242.2	22.8	22.6
0505720501	10.685340	41.266297	236.6	21.8	20.5
0505720601	10.686532	41.265788	230.8	21.9	21.9
0551690201	10.685436	41.266376	252.7	21.9	21.8
0551690301	10.684949	41.265549	246.9	21.9	21.7
0551690401	10.685264	41.266371	243.5	27.1	9.4
0551690501	10.686075	41.266356	236.8	21.9	21.3
0551690601	10.685709	41.265679	232.1	26.9	19.2
0600660201	10.684718	41.265592	254.1	18.8	18.7
0600660301	10.685422	41.265350	248.2	17.3	17.3
0600660401	10.685428	41.266005	243.7	17.2	17.2
0600660501	10.685658	41.266166	238.1	19.7	19.5
0600660601	10.686281	41.265839	233.5	17.3	17.3
0650560201	10.684482	41.265614	255.5	26.9	26.9
0650560301	10.685331	41.265653	249.5	33.4	33.3
0650560401	10.685800	41.265618	243.8	24.3	22.1
0650560501	10.685515	41.266252	238.3	23.9	23.9
0650560601	10.685947	41.265886	232.5	23.9	23.8
0674210201	10.684554	41.266374	254.5	20.9	20.8
0674210301	10.684424	41.266428	248.5	17.3	17.3
0674210401	10.684782	41.266029	244.0	19.9	19.9
0674210501	10.685569	41.265826	240.7	17.3	17.3
0674210601	10.684913	41.265902	235.0	26.0	20.4

\* Columns are: Observation ID, Right Ascension (degree), Declination (degree), Position Angle (degree), Exposure Time (ks), and Effective Time (ks).

mainly cataclysmic variables (CVs) and coronal active binaries (ABs). Empirically, we model the bright-point-source component with a power law. The X-ray emission of the CVs and ABs arises primarily from optically thin thermal plasma with temperature similar to that of the diffuse hot gas. So the separation of their contribution is not straightforward spectroscopically. Instead, we characterize the contribution with two *fixed* APEC models of the characteristic temperatures of 4.6 keV and 0.38 keV, respectively. These values are obtained from the spectral fitting to the unresolved emission from the small dwarf galaxy M32, which should not contain any significant diffuse hot gas. The luminosity of this stellar X-ray emission is approximately proportional to that of the stellar Ks-band emission:  $L_{0.5-2\text{keV}}/L_{Ks} = (4.7 \pm 0.4) \times 10^{27} \text{ erg s}^{-1} L_{\odot}^{-1}$  (Ge et al. 2015). Using the 2MASS<sup>7</sup> Ks-band data in the typical rectangular region ( $16' \times 4'$ ) where the RGS spectra are extracted (Figure 6), the X-ray luminosity, which determines the normalization parameters of the APEC models, is scaled accordingly. The spatial distribution of the contribution follows the extended stellar distribution traced by the Ks-band emission and is used to

<sup>7</sup> <https://www.ipac.caltech.edu/2mass/index.html>

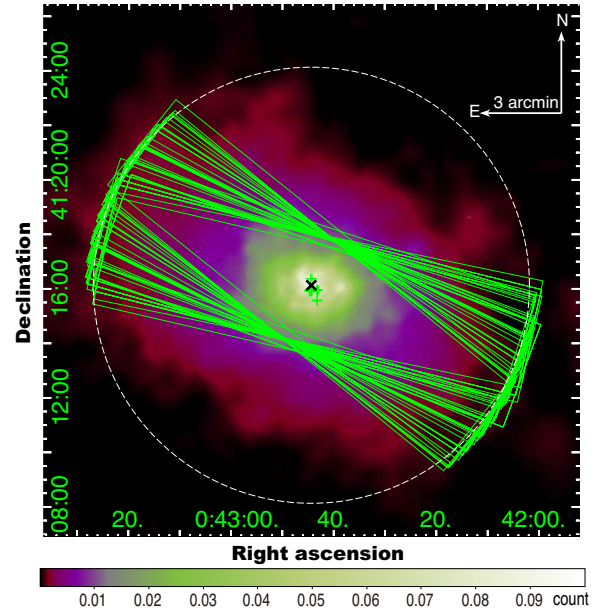


FIG. 6.— Chandra/ACIS 0.5-2 keV image of the diffuse emission intensity in the M31 bulge region. The white dash circle with a radius of  $8'$  ( $\sim 1.8$  kpc) outlines a region containing about 95% of the emission. The green rectangles ( $16' \times 4'$ ) represent the dispersion directions and the widths of our adopted spectral extraction regions of the 36 RGS observations and the green crosses show their telescope pointing centers. The black cross marks the position of the central supermassive black hole of the galaxy.

generate the broadened line profiles of the RGS spectra as described in Sec. 4.1. Specifically, we convolve the angular structure function of the Ks-band image in the rectangular region with the two APEC models via the XSpec script `rgsxsrsc`, which uses the central supermassive black hole's coordinates and the position angle of  $250^\circ$ . As a result, the contribution of the unresolved point sources to the RGS spectrum is determined.

We start with characterizing the X-ray emission from diffuse hot gas with a single-temperature APEC model. Unlike the unresolved-point-source component whose RGS line profile is modeled with the extended stellar distribution, the line profile of the hot gas component is determined by the spatial distribution of the gas itself. Figure 6 shows the 0.5–2 keV image of the diffuse emission intensity in M31, which is constructed from mosaicking 31 *Chandra*/ACIS observations (Li & Wang 2007), with the unresolved point source contribution scaled according to the Ks-band image and subtracted. The convolution is again carried out with `rgsxsrsc`. The foreground absorption with a column density of  $6.7 \times 10^{20} \text{ cm}^{-2}$  (Dickey & Lockman 1990) is assumed for all the spectral components: the bright point sources, the CVs and ABs, and the diffuse hot gas.

Figure 7 presents the best-fit APEC model of the RGS spectrum of the M31 bulge with a temperature of  $\sim 0.23$  keV. There are deviations: e.g., the OVII f line flux exceeds the model prediction significantly, as already noticed in Liu et al. (2010), which cannot be alleviated by simply adding more CIE plasma components. Here, we focus on the OVIII Ly $\alpha$  and OVII K $\alpha$  line complex (18–23 Å) in the spectrum. By dealing with transitions all from a single element, we avoid the complication that may be introduced by the uncertainties in the hot gas

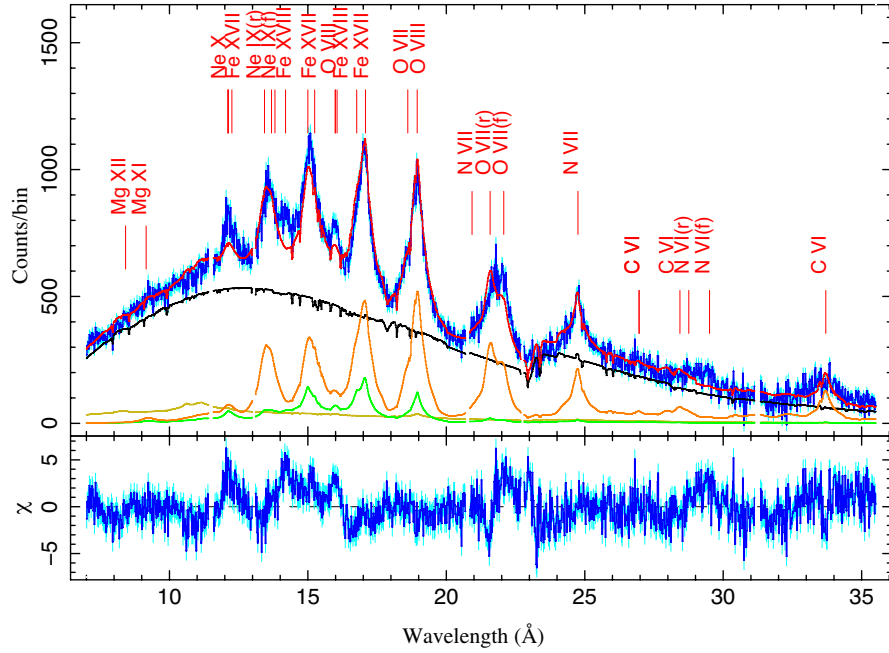


FIG. 7.— The combined RGS spectrum of the M31 bulge and the best-fit APEC model of optically thin plasma (red). The black curve is for the bright point sources, the green and yellow curves are for the unresolved ABs and CVs, and the orange curve is for the hot gas described with a single-temperature APEC model, respectively.

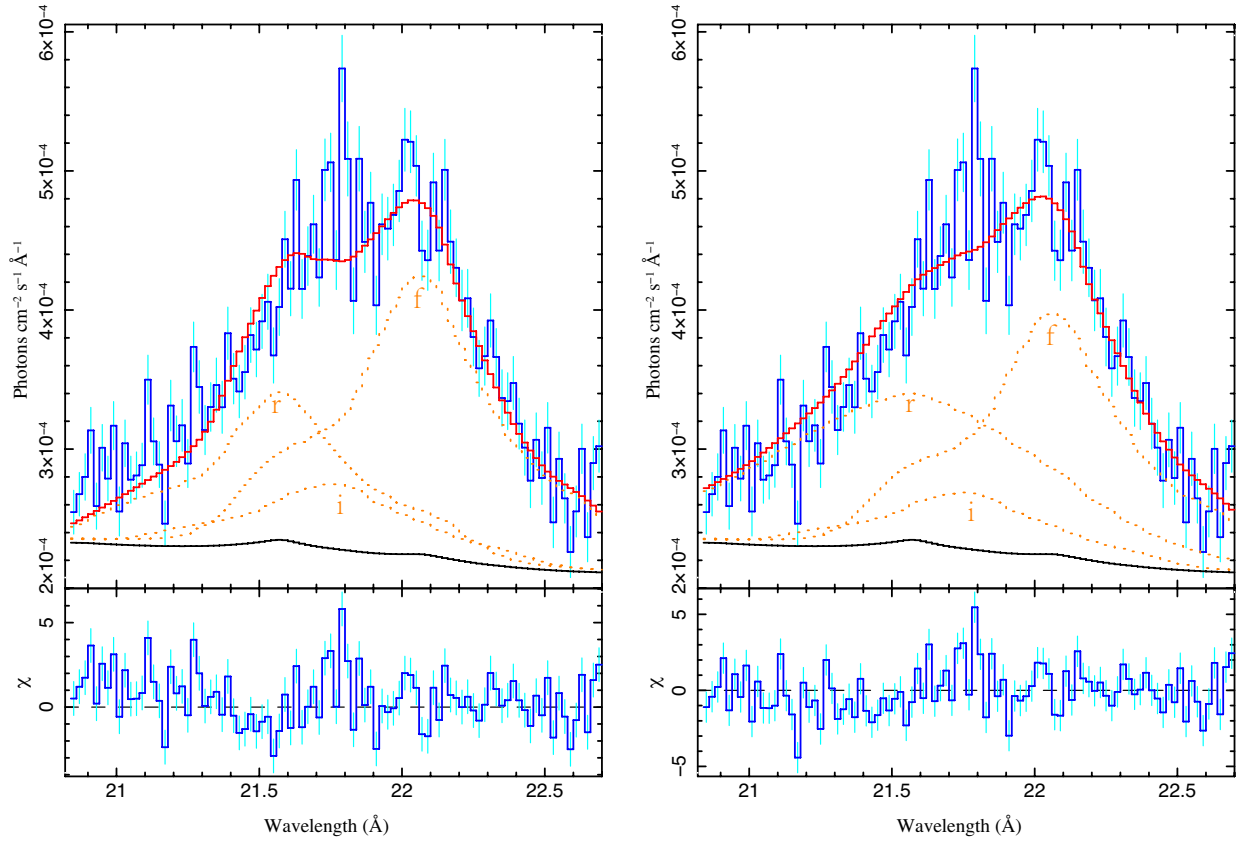


FIG. 8.— Model fits to the OVII complex. The left panel shows the fit with fixed intrinsically narrow Gaussians convolved with the angular structure function of the hot gas distribution, while the right panel has the OVII r line fitted with a broader Gaussian, which leads to a decrease of the  $\chi^2$  from 281 (left) to 241 (right) with 95 data bins. In both panels, the black curves represent the continuum, while the dotted lines labeled with “r”, “i”, and “f” are the modeled spectra of the OVII resonant, intercombination, and forbidden lines, respectively.



metal abundances.

To achieve a quantitative analysis, we measure the intensities of individual prominent oxygen lines (Table 1). With the background radiation, including the emission from all point sources and the continuum emission from the hot gas, fixed to the above best-fit model, each line is characterized with a Gaussian, which is convolved with the angular structure function of the diffuse X-ray image via `rgsxssrc`. The flux of the OVII intercombination line is scaled to that of the forbidden line with a fixed value of 0.225, which is nearly constant in the temperature range between  $10^6$ – $2 \times 10^7$  K. Because the wavelength separation between the two OVIII lines is less than 0.01 Å, which cannot be distinguished in the RGS spectrum, they are jointly fitted with one single Gaussian. The fitting results as shown in Figure 8a give the OVII G-ratio as  $2.39 \pm 0.21$ , which is significantly larger than what is expected in a CIE plasma (Fig. 9), and the OVII K $\alpha$ /OVIII Ly $\alpha$  ratio as  $1.68 \pm 0.08$ , which may be reproduced by a CIE plasma of a temperature  $\sim 2.5 \times 10^6$  K. However, the blue wing of the OVII r line is not well fitted and appears broader than the model profile.

Both the broader OVII r line and the high OVII G-ratio may be naturally explained by the RS effect, which primarily redistributes the line photons from the inner to the outer regions. This redistribution is opacity-dependent, and as a result, some of the OVII r photons with higher opacities can be scattered out of the extraction region. This leads to the decrease of the line flux (e.g., Fig. 3) or the increase of the G-ratio in the region (e.g., Fig. 5). The changed angular structure function of the extended OVII r emission map in turn leads to a broader OVII r line in the RGS spectrum. While the above analysis assumes intrinsically narrow Gaussians (with the widths fixed to 0.001Å), we allow the width to vary in the spectral fit, especially to the blue wing of the OVII r line (Figure 8b). The fit to the red wing at  $\sim 21.8$  Å is also improved, although there is still an apparent excess in the RGS spectrum with a significance of about  $2 \sigma$ . This excess cannot be explained by an enhanced intercombination line, because this would require a flux ratio between the forbidden and intercombination lines achievable for a plasma with density higher than  $10^9 \text{ cm}^{-3}$  (Porquet & Dubau 2000). Other weak lines (mainly OVII and OVI satellite lines) concentrate around 19 Å and 21.6Å, with little contribution to this feature. Thus the residuals, if real, would most likely be due to other physical reasons (e.g., a substructure such as a cavity in the center, which is not modeled in the present work) or just be pure noise. Therefore, the large FWHM of the model for the OVII r line (with a Gaussian width  $0.35 \pm 0.06$ Å), which is about 2.5 times that of the OVII f line, is very likely to result from the RS effect. With this new fit, we get the OVII G-ratio as  $1.25 \pm 0.10$  and the OVII K $\alpha$ /OVIII Ly $\alpha$  ratio as  $1.84 \pm 0.09$ . This latter ratio is grossly inconsistent with the CIE plasma of  $\sim 2.4 \times 10^6$  K, which should have the OVII G-ratio of  $\sim 0.8$  (Fig. 9).

If this RS effect is indeed important in changing the resonant line fluxes, the above temperature estimate from the line intensity ratio could then be strongly biased, however. Our adopted  $\beta$ -model distribution gives a total hydrogen column density of the hot gas to be

$\sim 1.5 \times 10^{20} \text{ cm}^{-2}$ . Assuming a solar abundance (Anders & Grevesse 1989) for now, the corresponding column density of oxygen is  $1.1 \times 10^{17} \text{ cm}^{-2}$ . In this case, the  $\tau$  value of OVIII Ly $\alpha$  is  $\lesssim 7$  for a CIE plasma at any temperature, even when the turbulent dispersion is negligible. This means that at most  $\sim 50\%$  of the OVIII flux may be scattered out of the extraction region according to our MC simulation (Fig. 10). The  $\tau$  value of the OVII r line, on the other hand, can be  $\gtrsim 10$  if the temperature is below 0.2 keV and even up to 70 around 0.1 keV. However, since the OVII G-ratio is  $\sim 1.25$ , roughly twice the lowest CIE value in a broad temperature range (Fig. 9a), the flux loss of the OVII r line from the extraction region should be less than  $\sim 50\%$ . With these flux uncertainties taken into account, the OVII K $\alpha$ /OVIII Ly $\alpha$  ratio varies between 1.2–2.6, suggesting that the temperature of the hot gas is still in a range of  $2$ – $3 \times 10^6$  K.

Given the temperature, as well as the spatial distribution of the hot gas and the distance of M31 (780 kpc), one could also estimate the oxygen abundance from the overall intensity. Of course, all these estimates can be strongly affected by the turbulent velocity dispersion, which reduces the RS optical depth. To measure the temperature, the oxygen abundance, and the velocity dispersion accurately, we need a spectrum model that accounts for the RS effect, as well as the spatial distribution of the hot gas.

#### 4.3. RS spectral model for the oxygen complex

Assuming that the hot gas is isothermal, chemically uniform, and spherically-symmetric with a  $\beta$ -model density distribution, we separate its emission into two parts: 1) the resonant-line component that may be significantly affected by the RS, and 2) the RS-free component for the rest of emission lines and the continuum, to which the optically-thin assumption applies. For this RS-free component (modeled like APEC minus the resonant lines), we just need to account for the spatial distribution of the plasma via a single convolution with a kernel built from the  $\beta$ -model. For the RS component, we calculate the line-dependent spatial distortion and flux loss according to the changes of surface brightness (SB) profile in the MC simulation. For computational efficiency, we pre-calculate this model in a 3-D grid of the temperature (in the range of  $10^{5.5}$ – $10^7$  K), metal abundance (or for oxygen alone in the present simple case; 0.1–1 solar), and turbulence Mach number (0–0.4) of the plasma. When the turbulence is isotropic, we can define the 3-D Mach number as  $M = \sqrt{3}\sigma_{\text{tu}}/C_s$  where  $C_s = \sqrt{\gamma kT/\bar{\mu}m_H}$  is the sound speed,  $\gamma = 5/3$ , and the mean atomic weight  $\bar{\mu}$  is taken to be 0.6.

In the present application, the model includes four resonant lines: OVII K $\beta$ , OVII K $\alpha$ , and OVIII Ly $\alpha$  (consisting of two lines). For each line and at each grid point,  $\tau$  can easily be calculated, and then the convolution kernel can be derived from the simulated SB profiles and also the telescope vignetting (e.g., Fig. 3). The normalization parameter of the model is the same as that of the APEC model: i.e.,  $\eta = \int n_e n_H dV/(4\pi d^2)$  (where  $d$  is the distance to M31). Here,  $\eta$  is readily estimated as  $6.6 \times 10^{11} \text{ cm}^{-5}$  based on the RGS extraction region of the  $\beta$ -model. We call this table model as the RS spectral model, and all the calculations are based on the atomic

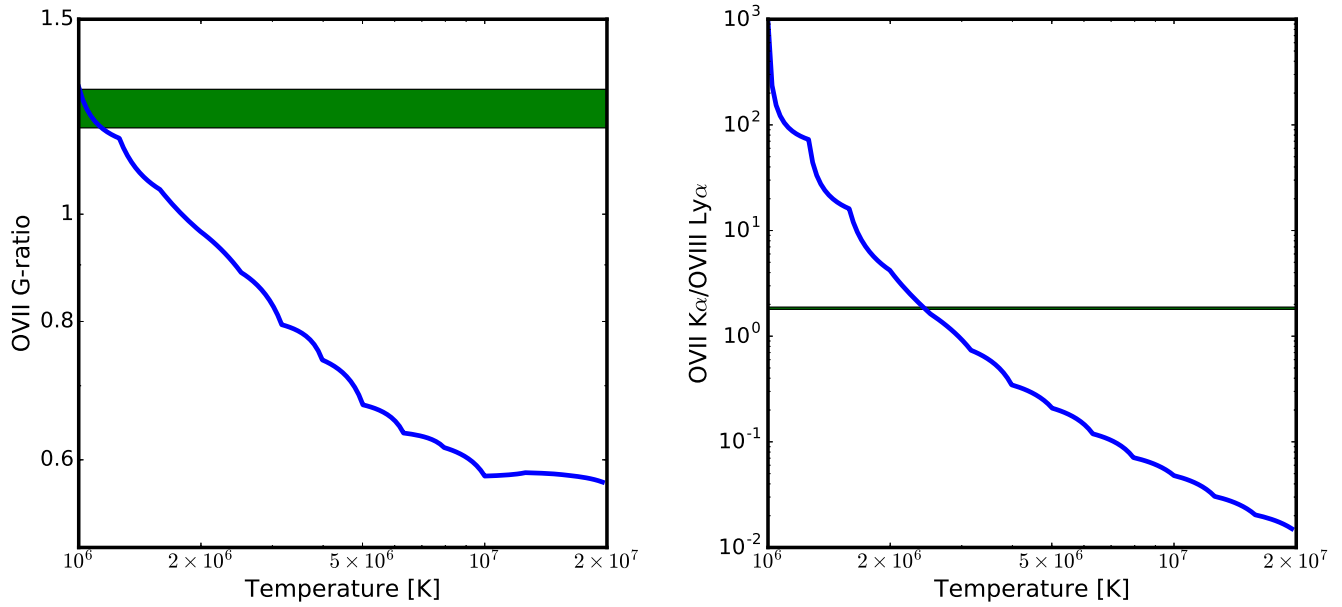


FIG. 9.— The OVII  $K\alpha$  triplet G-ratio (*left panel*) and the OVII  $K\alpha$ /OVIII  $Ly\alpha$  ratio (*right panel*) as functions of the temperature of CIE plasma, where the horizontal green bars mark the measured ratios from the RGS spectrum.

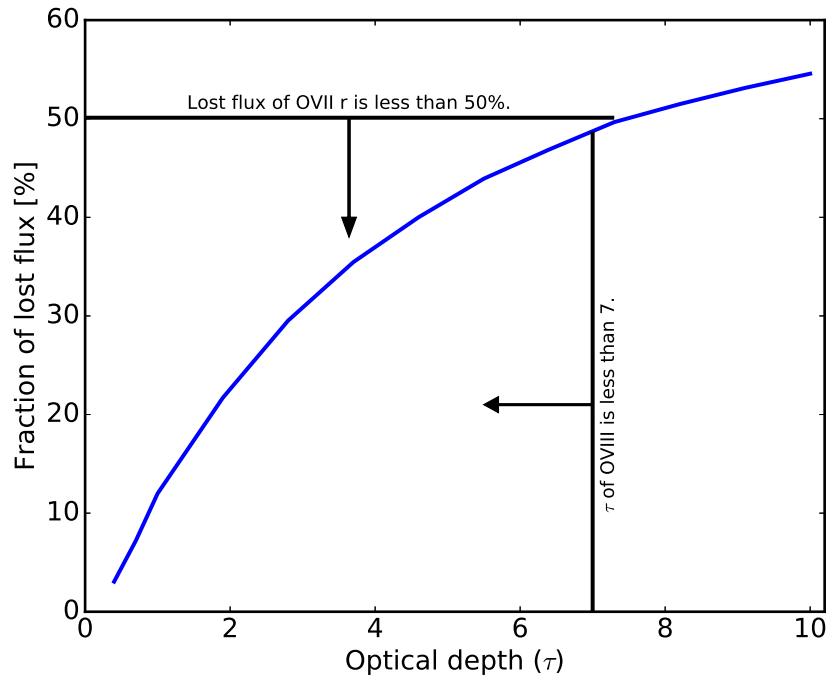


FIG. 10.— The RS flux loss in our spectral extraction region vs. the radial optical depth  $\tau$  according to our MC simulation. We estimate that the  $\tau$  value of the OVIII- $L\alpha$  line is less than 5 according to our modeled total column density and that the flux loss of the OVII  $K\alpha$  r line is less than 50% from the measured G-ratio.

database AtomDB (v3.0.2; Foster et al. 2012).

#### 4.4. Fitting and Discussion

Fig. 11 presents a fit of the RS spectral model to the OVIII+OVII complex of the RGS spectrum in the 18-23 Å range. Formally, the fit with  $\chi^2/d.o.f = 470/(233 - 3) \simeq 2.0$  does not seem to be satisfactory. While only statistical errors are included in the fit, systematic errors (though difficult to quantify) may be important for the spectral data, which have counting statistics, and may well dominate in this case. As such, we consider that the fit is quite reasonable, which constrains the temperature as  $0.195 \pm 0.001$  keV (or  $\sim 2.26 \times 10^6$  K), the oxygen abundance as  $0.51 \pm 0.02$  solar value, and the Mach number as  $0.17 \pm 0.02$  (all at the 90% confidence level). With the fitted temperature, we infer the sound speed of the hot gas as  $C_s \sim 228$  km s<sup>-1</sup>. The Mach number corresponds to an isotropic turbulence velocity dispersion of  $40 \pm 4$  km s<sup>-1</sup>. The characteristic  $\tau$  values of individual resonant lines corresponding to the best-fit spectral parameters are given in Table 1.

The above simple application of combining the simulations and spectral modeling demonstrates its feasibility. The most interesting result is the first constraint on the Mach number of the turbulence in the hot ISM of the M31 bulge. In particular, the estimate of the Mach number depends chiefly on the relative intensities of the lines, especially the G-ratio (which is obtained from the lines of the single ion species, or the OVII K $\alpha$  triplet), and should be quite robust. The best-fit Mach number is small, which seems to be broadly consistent with those estimated for massive elliptical galaxies (e.g., Werner et al. 2009; Ogorzalek et al. 2017) and clusters of galaxies (e.g., Hitomi collaboration 2016), within the measured uncertainties for individual objects or among them.

However, our results do depend on multiple assumptions, which need to be tested carefully. We have assumed the  $\beta$ -model inferred previously. The fitting results are generally insensitive to any small change ( $\lesssim 10\%$ ) of the parameters in the  $\beta$ -model. Parameters other than the Mach number, such as the temperature and abundance, are sensitive to various other assumptions that we have made in the modeling. The isothermality of the hot plasma is probably most problematic. Indeed, we find that our best-fit RS spectral model for the OVII+OVIII complex cannot fit the entire RGS spectrum. The iron emission lines in the spectrum seem to prefer a higher plasma temperature of  $\sim 0.6$  keV, for example. Therefore, a more sophisticated model, phenomenological and physical, is needed to explain the spectrum and to advance our understanding of the hot gas in the M31 bulge (Zhang et al. 2018a, in prep).

## 5. SUMMARY

Observational evidence is growing for the importance of the RS of soft X-ray resonant line emission by diffuse hot plasma in nearby galaxies, which affects the interpretation of its observed spectrum. Taking advantage of the modern computing power, we are developing a direct MC simulation scheme that will enable us to flexibly deal with the RS in the plasma, in principle, with an arbitrary spatial, thermal, chemical, and kinematic distribution. We have here reported the initial implementation of this scheme via dimensionless calculation to an isothermal, chemically uniform, and spherically symmetric plasma with a radial density distribution which can be characterized by a simple  $\beta$ -model. The simulation resulting from this scheme can be directly compared with those from existing calculations. In particular, we find that our results are consistent with those obtained from an iterative method allowed for a simplified treatment (Gilfanov et al. 1987).

Our spectral model dealing with RS effects simultaneously accounts for the optical depth-dependent spatial distortion and strength change of the line emission, consistent with previous calculations. This spectral model can be built for any specific spectral extraction region and from the simulation with an assumed spatial distribution of the plasma. We have fitted the model to the OVII/OVIII complex in the RGS spectrum of the inner bulge of M31, providing constraints on both isotropic turbulent velocity dispersion and temperature of the plasma as  $40 \pm 4$  km s<sup>-1</sup> and  $0.195 \pm 0.001$  keV.

However, we do find that the isothermal model is too simplistic to explain the entire RGS spectrum of the plasma. Therefore, further refining the modeling of the spectrum is needed to accurately measure the thermal, chemical, and kinematic properties of hot plasma. Extending the simulations to more physical models of the plasma distribution and to larger spectral ranges will enable us to study the RS effect in more realistic and complicated cases (e.g., galactic hot gaseous disks of various inclination angles).

## 6. ACKNOWLEDGMENTS

We appreciate the anonymous referee for constructive comments and Zheng Zheng for carefully reading the manuscript. We thank Shikui Tang, Hui Li, Wei Sun, and Xin Zhou for various technical helps in the study. We also thank Shawn Roberts for the help with the M31 data fit. Y.C. acknowledges the supports from the 973 Program grants 2017YFA0402600 and 2015CB857100 and NSFC grants 11773014, 11633007, 11851305, 11233001, and 10725312. S.Z. acknowledges the support of the China Scholarship Council and the supports from NSFC grants 11573070 and 11203080.

## REFERENCES

- Ahn, S.-H., Lee, H.-W., & Lee, H. M. 2000, *Journal of Korean Astronomical Society*, 33, 29  
 Anders, E., & Grevesse, N. 1989, *Geochim. Cosmochim. Acta*, 53, 197  
 Arnaud, M. 2009, *A&A*, 500, 103  
 Breitschwerdt, D., & Schmutzler, T. 1999, *A&A*, 347, 650  
 Cavaliere, A., & Fusco-Femiano, R. 1978, *A&A*, 70, 677  
 Cantalupo, S., Porciani, C., Lilly, S. J., & Miniati, F. 2005, *ApJ*, 628, 61  
 Churazov, E., Forman, W., Jones, C., Sunyaev, R., Böhringer, H. 2004, *MNRAS*, 347, 29  
 Churazov, E., Zhuravleva, I., Sazonov, S., & Sunyaev, R. 2010, *Space Sci. Rev.*, 157, 193  
 de Plaa, J., Zhuravleva, I., Werner, N., et al. 2012, *A&A*, 539, A34  
 Dickey, J. M., & Lockman, F. J. 1990, *ARA&A*, 28, 215  
 Dijkstra, M., Haiman, Z., & Spaans, M. 2006a, *ApJ*, 649, 14  
 Dijkstra, M., Haiman, Z., & Spaans, M. 2006b, *ApJ*, 649, 37  
 Dong, H., Li, Z., Wang, Q. D. 2016, *MNRAS*, 459, 2262

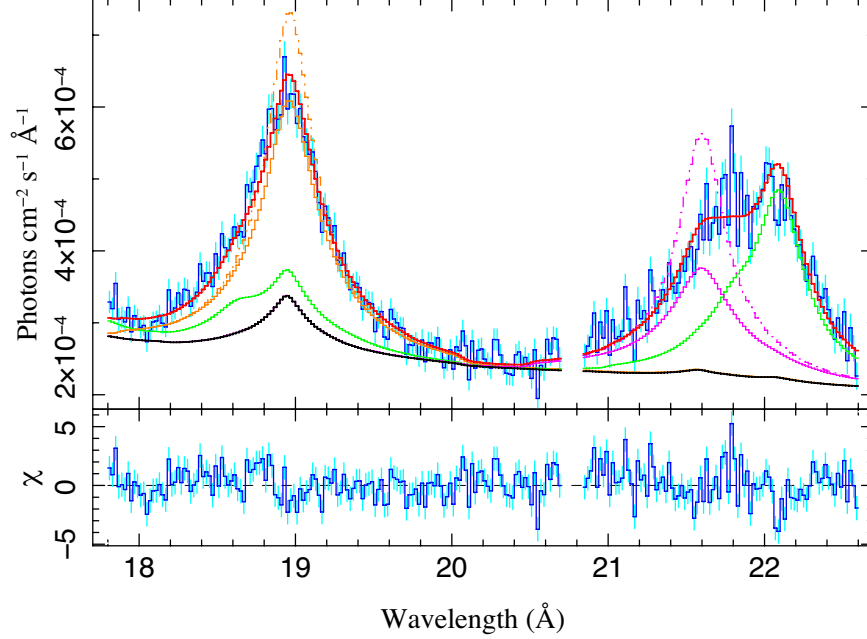


FIG. 11.— The RS spectral model (solid red line) best fitted to the OVIII+OVII complex of the RGS spectrum of the M31 bulge. Individual lines or combinations are illustrated separately: OVIII Ly $\alpha$  (orange), OVII resonance line (purple), and OVII K $\alpha$  intercombination+forbidden lines, OVII K $\beta$ , and other satellite lines (green). For comparison, the corresponding model resonant lines without the RS are shown (dash-dot). The black line represents the combined contribution from point sources and the hot gas continuum emission. The data at 20.75 Å, which are uncertain because of the presence of a CCD gap, are excluded in the spectral fit here.

- Field, G. B. 1959, *ApJ*, 129, 551  
 Foster, A. R., Ji, L., Smith, R. K., & Brickhouse, N. S. 2012, *ApJ*, 756, 128  
 Gabriel, A. H., & Jordan, C. 1969, *MNRAS*, 145, 241  
 Ge, C., Wang, Q. D., Tripp, T. M., Li, Z., Gu, Q., & Ji, L. 2016, *MNRAS*, 459, 366  
 Gilfanov, M. R., Syunyaev, R. A., & Churazov, E. M. 1987, *Soviet Astronomy Letters*, 13, 3  
 Gu, L., Mao, J., Costantini, E., & Kaastra, J. 2016, *A&A*, 594, A78  
 Hamilton, D. R. 1947, *ApJ*, 106, 457  
 Hitomi Collaboration, et al. 2016, *Nature*, 535, 117  
 Hitomi Collaboration, Aharonian, F., Akamatsu, H., et al. 2018, *PASJ*, 70, 10  
 Li, Z., & Wang, Q. D. 2007, *ApJ*, 668, L39  
 Li, Z., Wang, Q. D., & Wakker, B. P. 2009, *MNRAS*, 397, 148  
 Liu, J., Wang, Q. D., Li, Z., & Peterson, J. R. 2010, *MNRAS*, 404, 1879  
 Liu, J., Mao, S., & Wang, Q. D. 2011, *MNRAS*, 415, L64  
 Mihalas, D. 1978, *Stellar Atmospheres* (San Francisco: W.H. Freeman and Company)  
 Molnar, S. M., Birkinshaw, M., & Mushotzky, R. F. 2006, *ApJ*, 643, L73  
 Ogorzalek, A., Zhuravleva, I., Allen, S. W., et al. 2017, *MNRAS*, 472, 1659  
 Porquet, D., & Dubau, J. 2000, *A&AS*, 143, 495  
 Porquet, D., Dubau, J., & Grosso, N. 2010, *Space Sci. Rev.*, 157, 103  
 Ranalli, P., Comastri, A., Origlia, L., & Maiolino, R. 2008, *MNRAS*, 386, 1464  
 Sazonov, S. Y., Churazov, E. M., & Sunyaev, R. A. 2002, *MNRAS*, 333, 191  
 Segers, M. C., Oppenheimer, B. D., Schaye, J., & Richings, A. J. 2017, *MNRAS*, 471, 1026  
 Wang, Q. D., Yao, Y., Tripp, T. M., et al. 2005, *ApJ*, 635, 386  
 Wang, Q. D. 2010, *Proceedings of the National Academy of Science*, 107, 7168  
 Werner, N., Zhuravleva, I., Churazov, E., et al. 2009, *MNRAS*, 398, 23  
 Xu, H., Kahn, S. M., Peterson, J. R., et al. 2002, *ApJ*, 579, 600  
 Zanstra, H. 1949, *Bull. Astron. Inst. Netherlands*, 11, 1  
 Zhang, S., Wang, Q. D., Ji, L., et al. 2014, *ApJ*, 794, 61  
 Zheng, Z., & Miralda-Escudé, J. 2002, *ApJ*, 578, 33  
 Zhuravleva, I. V., Churazov, E. M., Sazonov, S. Y., et al. 2010, *MNRAS*, 403, 129  
 Zhuravleva, I. V., Churazov, E. M., Sazonov, S. Y., Sunyaev, R. A., & Dolag, K. 2011, *Astronomy Letters*, 37, 141  
 Zhuravleva, I., Churazov, E., Sunyaev, R., et al. 2013, *MNRAS*, 435, 3111

## APPENDIX

### APPENDIX: COMPARISON WITH ITERATION METHOD

Gilfanov et al. (1987) present an iterative method to calculate the RS effect under the assumption of small optical depth. As a general situation, the emissivity can be determined iteratively from the one with no scattering to the one with  $n$ th scattering:

$$j_{\nu}^{(n)}(r) = j_{\nu}^{(n-1)}(r) + \frac{\phi_{\nu}}{4\pi} n_i(r) \int d\Omega' \int_0^{+\infty} d\nu' s(\nu') \int_{-\infty}^0 d\xi j_{\nu'}^{(n-1)}(r_{\xi}) e^{-\tau_{\nu'}(\xi)}, \quad (\text{A1})$$

where  $j_{\nu}^{(n)}(r)$  denotes the emission coefficient after the  $n$ th scattering,  $\phi_{\nu} = \exp(-x^2)$  is the line profile function,  $s(\nu')$  is the cross section of the scattering, and  $r_{\xi} = \sqrt{r^2 + \xi^2 - 2r\xi\mu'}$  (with  $\mu'$  the cosine of the angle between the radial vector and the incident direction).

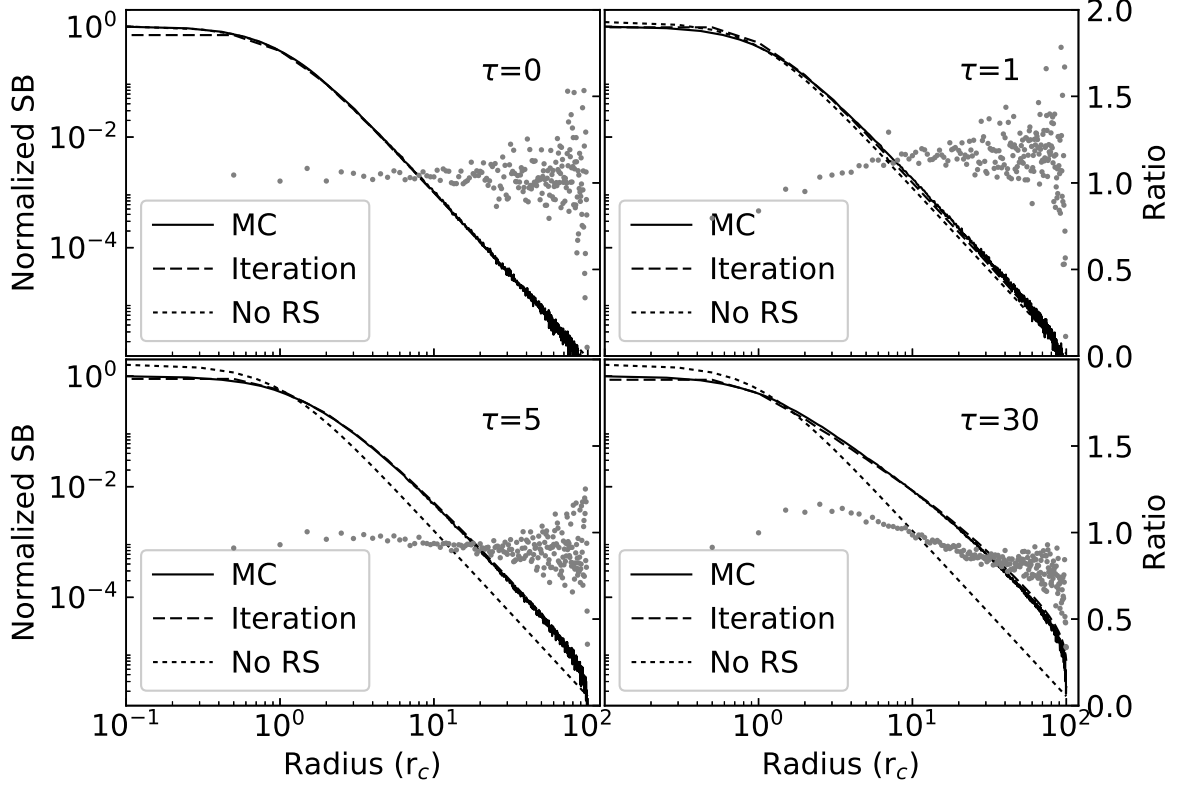


FIG. 12.— Comparison of resonant line surface brightness profiles obtained with two methods: the solid lines demonstrate the MC simulation results, while the dashed lines demonstrate the iterative calculation results. The grey dots represent the ratios between the MC and iteration results (with the scale shown on the right side of the figure). Both results are obtained for the hot gas distribution following the  $\beta$ -model with  $\beta=2/3$ . The four panels show the cases of different  $\tau$  values. For reference, the brightness profile for  $\tau=0$  (i.e. no RS), obtained from numerical integration of emission measure  $\int n_e n_{\text{ion}}(Z) dl$  along the line of sight, is plotted in all panels.

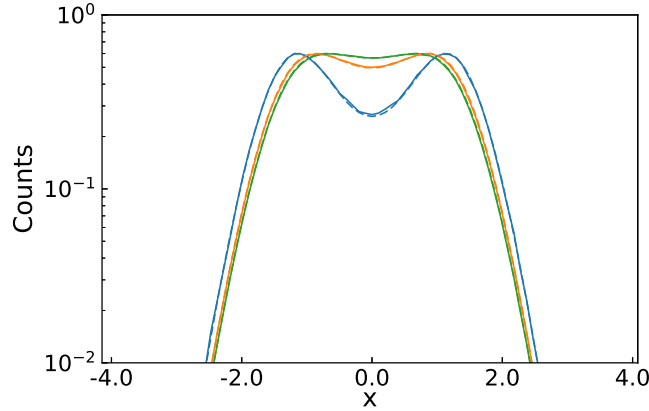


FIG. 13.— Comparison of the resonant line profiles obtained with two methods, assuming the same  $\beta$ -model as in Fig.12, but for  $\tau=5$  only. The solid and dashed lines are obtained from the MC simulation and iterative calculation, respectively. The line profiles of the emission within projected radii  $1r_c$ ,  $5r_c$ , and  $10r_c$  are shown in *blue*, *red*, and *green*, respectively. In the simulation,  $10^8$  photons are calculated. No smoothing is applied to the line profiles.

We consider the scattering of resonant line emission in an isothermal hot gas of  $\beta$ -model distribution with  $\beta=2/3$  like that used in Gilfanov et al. (1987), but with a cutoff  $r_{\text{cut}}=100r_c$ . For a comparison between the two methods, we make the MC simulation with the simplification used in the iteration calculation. Namely, isotropic scattering is considered, only the first term of the right hand side of Eq.(6) is used for the Voigt function, a Gaussian distribution instead of Eq.(14) is used for the parallel velocity component, and a Gaussian distribution instead of Eq.(7) is used for the frequency of the scattered photons. A comparison of the radial brightness profiles obtained from the iterative method and our MC simulation method for various  $\tau$  values is shown in Fig. 12. The brightness profiles from the two methods are in a good agreement. The ratios between the MC and iteration methods are generally close to unity,

except in the region near the boundary. Near the boundary, the RS numbers are relatively low, which increases the statistical noise. Moreover, the photons in our iterative calculation include those incident from outside the boundary (leading to an increase in the intensity). In contrast, no such photon is included in the MC calculation. The decrease in the ratios due to this difference is apparent near the boundary in the large optical depth cases, as seen in the bottom-right panel of Fig. 12. In addition, the resolution in the iterative calculation is relatively low and is largely limited by the computing power, which also contributes to the discrepancy between the two methods.

Fig. 13 presents the line profiles for the emission within projected radii  $1r_c$ ,  $5r_c$ , and  $10r_c$ , respectively, for the radial optical depth  $\tau = 5$  obtained from the two methods. The line profiles obtained from the simulation match those from iterative calculation reasonably well. The line profile from the central  $1r_c$  region exhibits double-peak shape; similarly to Gilfanov et al.'s (1987) case for the geometric center, the two peaks are at  $x \sim \pm 1.2$ . The shape of the emission line from the entire region (within  $100r_c$ ) is also very similar to the one obtained by Gilfanov et al. (1987).